

Parametrization of transition-metal Fermi-surface data*

J. B. Ketterson

Argonne National Laboratory, Argonne, Illinois 60439
and Northwestern University, Evanston, Illinois 60201

D. D. Koelling, J. C. Shaw,[†] and L. R. Windmiller

Argonne National Laboratory, Argonne, Illinois 60439

(Received 17 April 1974)

The phase shifts associated with a muffin-tin approximation of the crystal potential were used as parameters to represent the Fermi surface of the body-centered-cubic transition metals molybdenum and tungsten. The band-structure formalism employed was the relativistic Korringa-Kohn-Rostoker method and the phase-shift parameters were determined by a least-squares fit to extremal cross-sectional areas obtained from de Haas-van Alphen data. Five-parameter fits which employed the $s_{1/2}$, $p_{1/2}$, $p_{3/2}$, $d_{3/2}$, and $d_{5/2}$ phase shifts had root-mean-square errors which exceeded the estimated experimental error. Inclusion of the f phase shifts did not significantly reduce the discrepancy. Therefore, a formalism was developed and applied to include the nonspherical (inside-muffin-tin) corrections of the potential with the fits truncated at d -wave scattering. With the additional two parameters thus introduced an rms error consistent with the experimental error was obtained. As in the earlier work on noble metals, the rms error was found to be quite insensitive to the value of the Fermi energy used.

I. INTRODUCTION

There exists a growing body of very precise experimental information, chiefly from de Haas-van Alphen (dHvA) experiments, on the Fermi surface of transition metals.¹ It is thus necessary to condense such data into small parameter sets which, hopefully, will yield some insight into the underlying physics. An additional benefit can be obtained if the parametrization technique is limited (by the underlying physics) so that it cannot fit any arbitrary Fermi surface; in this case attempts to construct a surface from improperly interpreted data would yield a poor representation and thus suggest a re-examination. While pseudopotential methods have been quite successful in the parametrization of the Fermi surface (and band structure) of simple metals,² a corresponding band-structure based formalism for transition metals has not yet been demonstrated. It has been suggested that the phase shifts associated with a muffin-tin approximation to the periodic crystal potential are an excellent parameter set.³ This is credible since this approximate form of the potential is regularly used in the augmented-plane-wave⁴ (APW) and Korringa-Kohn-Rostoker^{3,5} (KKR) band-structure calculation schemes with good success. In this paper we present an application of this approach to Mo and W. Finding it to be inadequate, we augment the parameter set by including the form of the nonspherical muffin-tin corrections which are rigorously correct only inside the muffin-tin spheres. The formalism used is, however, a severe truncation of a more general formulation which uses a sphere circumscribed on the unit cell with a step function limiting the effects of the potential to the cell.⁶ The most

significant point, however, is that it introduces an adequate and well-defined representation of the non-muffin-tin effects where the parameter fitting can compensate for truncation errors.

In Sec. II, we review the application of the phase-shift parametrization in the muffin-tin form and, in Sec. III, we present the modifications necessary to include a non-muffin-tin correction. The application of these techniques to Mo and W are then presented and compared in Sec. IV. We conclude in Sec. V by comparing these parametrizations to others currently in use and speculating about the effect of improved experimental data on the model.

II. PHASE-SHIFT PARAMETRIZATIONS

In the KKR method, the functions $E_n(\vec{k})$ where E , \vec{k} , and n are the energy, wave vector, and band index, respectively, are solutions of the secular equation

$$\det(M) = 0, \quad (1a)$$

$$M \equiv B_{l'm', l'm}(\vec{k}, E) + E^{1/2} \delta_{ll'} \delta_{mm'} \cot \eta_l(E). \quad (1b)$$

$B_{l'm', l'm}(\vec{k}, E)$ are the "structure constants" and E is measured relative to the potential outside the muffin-tin spheres. We require $|\eta_l| \leq \frac{1}{2}\pi$ which are referred to as the reduced phase shifts. When fitting Fermi surface data, a value of E is selected (the Fermi energy parameter) and the phase shifts η_l are adjusted such that the constant energy surfaces are a best fit to experimental data.

Assume that we have available a set of experimental areas A_i^E whose associated orbits sample the Fermi surface in some favorable manner (to be discussed later). Let $A_i^C(\vec{\eta})$ be the area (corresponding to A_i^E) calculated from the KKR formal-

ism for the set of phase shifts $\vec{\eta} = \{\eta\}$. Also associated with A_i are, of course, the parameters which define the orbit (magnetic field direction, band index, and the coordinate of the orbit center). We define the error function

$$\Delta^2(\vec{\eta}) = \frac{1}{N} \sum_{i=1}^N \left(\frac{A_i^C(\vec{\eta}) - A_i^E}{A_i^E} \right)^2, \quad (2)$$

where N is the total number of areas included in the fit. Differentiation of Eq. (2) to determine a minimum yields

$$\frac{\partial \Delta^2}{\partial \vec{\eta}} = 0 = \frac{2}{N} \sum_{i=1}^N \frac{A_i^C(\vec{\eta}) - A_i^E}{(A_i^E)^2} \frac{\partial A_i^C(\vec{\eta})}{\partial \vec{\eta}} = 0. \quad (3)$$

Expanding $A_i^C(\vec{\eta})$ through linear terms in a Taylor series about $\vec{\eta}_0$ (a point presumed to be near the minimum), we obtain

$$\vec{T} \cdot \delta \vec{\eta} + \vec{X} = 0, \quad (4a)$$

where

$$\vec{X} = \frac{2}{N} \sum_{i=1}^N \frac{A_i^C(\vec{\eta}_0) - A_i^E}{(A_i^E)^2} \frac{\partial A_i^C}{\partial \vec{\eta}} \Big|_{\vec{\eta}=\vec{\eta}_0}, \quad (4b)$$

$$\vec{T} = \frac{2}{N} \sum_{i=1}^N \frac{1}{(A_i^E)^2} \frac{\partial A_i^C}{\partial \vec{\eta}} \Big|_{\vec{\eta}=\vec{\eta}_0} \frac{\partial A_i^C}{\partial \vec{\eta}} \Big|_{\vec{\eta}=\vec{\eta}_0}, \quad (4c)$$

and

$$\delta \vec{\eta} = \vec{\eta} - \vec{\eta}_0.$$

In performing the iterations one cannot always go the "full step" in $\delta \vec{\eta}$ resulting from the solution of Eq. (4). For the initial iterations a step of $\frac{1}{4}$ or $\frac{1}{2}$ of the predicted step was usually sufficient to ensure stability and convergence. A sign that one is sufficiently close to the minimum of $\Delta^2(\vec{\eta})$ as to permit a full step is that the predicted rms error $\Delta^2(\vec{\eta} + \delta \vec{\eta}) = \Delta^2(\vec{\eta}) + \frac{1}{2} \vec{X} \cdot \delta \vec{\eta}$ of the succeeding iteration not change on successive iterations.

The area and its phase shift derivative are given, in a cylindrical coordinate system aligned with the field, by⁷

$$A_i^C = \frac{1}{2} \int_0^{2\pi} k_{\perp}^2(k_{\parallel}, \vec{\eta}) d\theta \quad (5)$$

and

$$\frac{\partial A_i^C}{\partial \eta_j} = \int_0^{2\pi} k_{\perp} \frac{\partial k_{\perp}}{\partial \eta_j} d\theta, \quad (6)$$

where k_{\parallel} measures the displacement of the orbit center along the magnetic field from the origin and k_{\perp} is the radius, in the plane of the orbit, measured from the orbit center. The derivative required for Eq. (6) may be calculated analytically.⁸ Let $\lambda^{(\vec{n})}$ be the eigenvalue of the matrix \vec{M} [see Eq. (1)] associated with the band giving rise to the desired sheet of the Fermi surface. [Although the index \vec{n} of this eigenvalue is not identical to the band index, each sheet of the surface has an eigenvalue index associated with it. An exception to this rule

occurs when, on tracing an orbit around the surface, the Fermi radius passes through a free-electron singularity $E = (k + K_n)^2$; K_n is a reciprocal-lattice vector. In that case the eigenvalue index will change by one. Our programs are designed to automatically change the eigenvalue index on crossing such free electron singularities.] From the chain rule for partial derivatives we have

$$\frac{\partial k_{\perp}}{\partial \eta_j} = - \left(\frac{\partial \lambda^{(\vec{n})}}{\partial \eta_j} \right) / \left(\vec{k}_{\perp} \cdot \frac{\partial \lambda^{(\vec{n})}}{\partial \vec{k}} \right). \quad (7)$$

The derivatives of the eigenvalue with respect to $\vec{\eta}$, \vec{k} , and E (which is required if Fermi velocities are desired) are calculated by the Hellman-Feynman theorem

$$\frac{\partial \lambda^{(\vec{n})}}{\partial \eta_j} = \sum_{i,m} V_i^{(\vec{n})*} \frac{\partial M_{im}}{\partial \eta_j} V_m^{(\vec{n})}, \quad (8a)$$

$$\frac{\partial \lambda^{(\vec{n})}}{\partial \vec{k}} = \sum_{i,m} V_i^{(\vec{n})*} \frac{\partial M_{im}}{\partial \vec{k}} V_m^{(\vec{n})}, \quad (8b)$$

$$\frac{\partial \lambda^{(\vec{n})}}{\partial E} = \sum_{i,m} V_i^{(\vec{n})*} \frac{\partial M_{im}}{\partial E} V_m^{(\vec{n})}, \quad (8c)$$

where $\vec{V}^{(\vec{n})}$ is the eigenvector associated with $\lambda^{(\vec{n})}$ of the secular matrix \vec{M} . The derivatives of the secular matrix M with respect to $\vec{\eta}$, \vec{k} , and E are computed analytically. For maximum efficiency the diagonalization routines calculate only the desired eigenvalue and eigenvector. To perform the integrations of Eqs. (5) and (6) we must be able to both locate the surface at a given angle and advance to the next vector in the orbit. These two operations are accomplished using "return-to-surface" and "stepping" routines described elsewhere.^{7,8} For both Mo and W, it was necessary to add an improvement to the orbit tracing package⁹ which allowed one to follow orbits where the orbit doubles back on itself as a function of angle. This allows us to treat the electron jack surface where the Fermi radius is multivalued for some angles. This was done by stepping with constant line segments instead of constant angular increments. This, however, necessitated giving up Simpson's rule integration and using a trapezoidal rule instead. As a result, the angular integration option was retained and selected wherever possible.

Nonrelativistic calculations of this type with the truncated parameter set involving only the s , p , and d phase shifts have been very successful in parametrizing the noble-metal Fermi surfaces of Cu, Ag, and Au.^{8,10} It is well known, however, that relativistic effects become increasingly important in the heavier metals. The spin-independent effects (mass-velocity, Darwin, etc.) are actually included by the parameter fitting into the nonrelativistic form. Thus it is the spin-orbit interaction which is the only new effect brought about by the inclusion of

relativistic effects. (This is true only when one is parametrizing. If the phase shifts are to be calculated from a potential, one must include the spin independent effects or one will get an s - d shift.¹¹) The effect of the spin-orbit interaction becomes particularly significant in the vicinity of degeneracies which are lifted relativistically. The noble metal surface does not pass near such degeneracies (which accounts for the success in Ag and Au); for the transition metals the inclusion of relativistic effects is usually necessary to get the correct topology.

The inclusion of relativistic effects leads to the relativistic KKR (RKKR) secular matrix¹²⁻¹⁴

$$M = B_{\kappa\mu, \kappa'\mu'}(\vec{k}, E) + (E)^{1/2} \delta_{\kappa\kappa'} \delta_{\mu\mu'} \cot\eta_{\kappa}(E), \quad (9)$$

where $B_{\kappa\mu, \kappa'\mu'}$ are sums over the nonrelativistic structure factors $B_{lm, l'm'}$ with appropriate Clebsch-Gordan coefficients. The phase shifts $\eta_{\kappa}(E)$ characterize the scattering of electrons by the muffin-tin potential using the two-component Pauli Hamiltonian,¹⁵ with spin orbit included. The quantum numbers j and l are specified by κ according to the rules:

$$\begin{aligned} j = l - \frac{1}{2}, \quad l = \kappa \quad (\kappa > 0), \\ j = l + \frac{1}{2}, \quad l = -(\kappa + 1) \quad (\kappa < 0), \end{aligned} \quad (10)$$

with $\mu = m_j$, the azimuthal quantum number. Thus $\kappa = -1, 1, -2, 2,$ and -3 correspond to the $s_{1/2}$, $p_{1/2}$, $p_{3/2}$, $d_{3/2}$, and $d_{5/2}$, respectively. With this

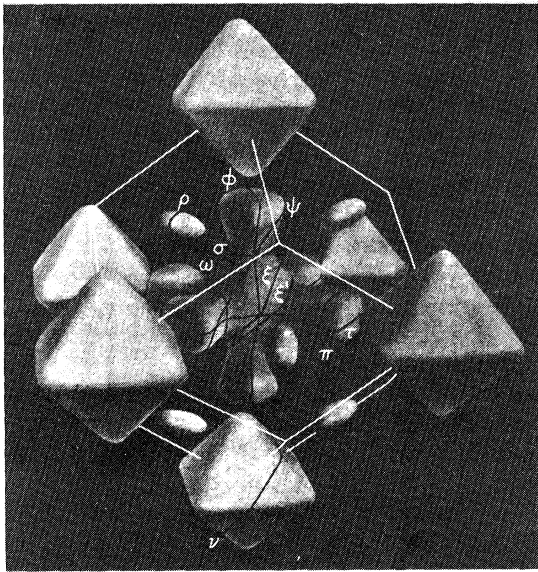


FIG. 1. Perspective sketch of the Fermi surface of W (after Girvan, Gold, and Phillips). The white lines show the Brillouin-zone edges while the dark lines show various extremal orbits. Only the ellipsoids associated with the front faces of the zone are drawn.

relatively minor modification, the relativistic parametrization is carried out in exactly the same way as the nonrelativistic case.

We attempted an application to Mo of this procedure based on the assumption of a muffin-tin-like potential excluding the σ and π orbits (Fig. 1). The resulting rms error was $\sim 1.6\%$ and the predicted values of the σ and π orbits differed from experiment by several percent. The σ and π orbits sample low symmetry regions of the zone where, due to hybridization, nonspherical terms would make the largest contribution. Calculations in which f -wave scattering was added did not decrease the error substantially (one then has a total of seven parameters just as in the nonspherical-muffin-tin case). Clearly, the inclusion of the nonspherical terms is an important physical effect which is essential to obtain a fit to the data within experimental error. This result points up one important additional fact about the phase shift parametrization method. Since the technique is limited by the underlying physics in the Fermi surfaces that it can parameterize, useful checks can be made on the interpretation of the data as to assignment of dHVA frequencies to specific extremal areas.

Application of the nonrelativistic muffin-tin formalism to W gave an rms error of $\sim 4\%$ using s , p , and d phase shifts. The inclusion of relativistic effects using $s_{1/2}$, $p_{1/2}$, $p_{3/2}$, $d_{3/2}$, and $d_{5/2}$ phase shifts decreased the error by a factor of 8, clearly, as expected, relativistic effects are very important in the heavier transition metals. The application of the non-muffin-tin relativistic formalism further reduced the error by a factor 2.

III. NON-MUFFIN-TIN PARAMETRIZATION

Corrections to the muffin-tin model are of two types: (a) *nonspherical* contributions to the potential inside the muffin-tin radius, and (b) *nonflat* behavior in the remainder (interstitial region) of the unit cell (there is, of course, some arbitrariness in this separation). For the case of the APW method, techniques for treating both the nonspherical¹⁶ and nonflat¹⁷ contributions have been developed. For the KKR formalism the nonflat contribution destroys the simple structure of the secular equations.¹⁸ However, John, Lehmann, and Ziesche¹⁹ have shown that the inclusion of nonspherical muffin-tin scatters in the KKR technique can be accomplished with only a minor modification of Eq. (1) or (9). It was desired to include non-muffin-tin effects with a minimum of modification to our existing computer programs; therefore we have adopted the formalism of John *et al.*¹⁹ Since we are fitting experimental data, some of the nonflat contributions will presumably be adsorbed into our parameter set. As mentioned in Sec. I this can alternatively be viewed as a truncation of a general procedure in which there

is no interstitial region. In any case, evidence indicates that for the bcc transition metals the non-spherical terms inside the muffin-tin spheres are the principal correction.²⁰

The procedure of John *et al.*¹⁹ is based on the method of partial waves developed by Demkov and Rudakov to treat nonspherical scatterers.²¹ The scattering from nonspherically symmetric muffin-tin potentials may be described in terms of generalized phase shifts η_λ and corresponding partial-wave amplitudes $A_{L\lambda}$ associated with the eigenvalues and eigenvectors of the angular momentum representation of the scattering matrix $S_{LL'}$ through

$$\sum_{L'} S_{LL'} A_{L'\lambda} = e^{i\eta_\lambda} A_{L\lambda}, \quad (11)$$

where the notation L implies the pair l, m_l ; both η_λ and $A_{L\lambda}$ depend only on the energy. Alternatively, the phase shifts and amplitude may be defined in terms of the scattered-state wave function outside the muffin-tin sphere

$$\varphi_\lambda(\vec{r}) = \sum_L [\sin\eta_\lambda n_L(\vec{r}) - \cos\eta_\lambda j_L(\vec{r})] A_{L\lambda}, \quad (12a)$$

where

$$j_L(\vec{r}) \equiv j_l(E^{1/2}r) Y_L(\hat{r}) \quad (12b)$$

and

$$n_L(\vec{r}) \equiv n_l(E^{1/2}r) Y_L(\vec{r}). \quad (12c)$$

The index λ numbers the irreducible representations associated with the symmetry group of the scatterer.

The generalized KKR secular equation derived by John *et al.*¹⁹ for nonspherical muffin-tin scatterers which involves these generalized phase shifts and amplitudes is given by

$$M = \sum_{L, L'} \bar{A}_{\lambda L} B_{LL'} A_{L'\lambda} + (E)^{1/2} \delta_{\lambda\lambda'} c c' \eta_\lambda, \quad (13)$$

where, for simplicity, we have reverted to the non-relativistic case. It is convenient to write the \bar{A} matrix as the product

$$\bar{A} = \bar{R} \cdot \bar{A}', \quad (14)$$

where \bar{R} is a matrix which, when operating on the spherical harmonic basis states, generates the appropriate linear combination of basis functions which transform as irreducible representations (ordered according to increasing L). The A' matrix then has the effect of coupling the equivalent irreducible representations.

The example of interest here is the case of cubic symmetry. The first two terms in the cubic harmonic expansion of the crystal field may be written²²

$$V(r) = V_0(r) + V_4(\vec{r}) + \dots, \quad (15a)$$

where

$$V_4(\vec{r}) = v_4(r) \left\{ \left(\frac{5}{24} \right)^{1/2} [Y_{44}(\hat{r}) + Y_{44}^-(\hat{r})] \right.$$

$$\left. + \left(\frac{7}{12} \right)^{1/2} Y_{40}(\hat{r}) \right\}. \quad (15b)$$

$V_4(\vec{r})$ transforms as Γ_4 , of course. In the following we will limit ourselves to $l^{\max} = 2$ and first discuss the nonrelativistic problem. The s and p states of the spherical representation are irreducible under the cubic group and correspond to the Γ_1 and $\Gamma_{15'}$ representations, respectively. The d states are reducible, however, and are split by the V_4 term into $\Gamma_{25'}(T_{2g})$ and $\Gamma_{12}(E_g)$ states. Thus \bar{R} is a unit matrix except in a portion of the d block where it acts to generate the T_{2g} and E_g states; this matrix is given in the Appendix. Since there are no equivalent representations for $l \leq 2$ the A' matrix is the unit matrix. A Fermi surface parametrization for nonspherical potentials will then involve the four phase shifts η_{Γ_1} , $\eta_{\Gamma_{15'}}$, $\eta_{\Gamma_{25'}}$, and $\eta_{\Gamma_{12}}$ as opposed to η_s , η_p , and η_d for the spherical case.²³

In the relativistic case, we again confine ourselves to $l^{\max} \leq 2$. Instead of the quantum number $\{l, m\}$ in the previous equations we employ κ and μ , or equivalently, j and m_j . The spherical $s_{1/2}$, $p_{1/2}$, $p_{3/2}$, and $d_{3/2}$ states are irreducible under the cubic group and correspond to the Γ_6^+ , Γ_6^- , Γ_8^- , and Γ_8^+ representations, respectively. The spherical $d_{5/2}$ states are a mixture of the Γ_8^+ and Γ_7^+ representations. The R matrix is then a unit matrix except for a 6×6 block operating on the $d_{5/2}$ states to produce the unmixed Γ_8^+ and Γ_7^+ states. Contrary to the nonrelativistic case, the \bar{A}' matrix is no longer a unit matrix in that there are now two equivalent Γ_8^+ representations which are coupled by the spin-orbit interaction or the V_4 terms in the potential (since $[V_4, \vec{\sigma} \cdot \vec{L}] \neq 0$, a basis set which diagonalizes both effects does not exist). If the \bar{R} matrix is constructed such that the two Γ_8^+ representations are identical (not just equivalent), then the \bar{A}' matrix is a real matrix constructed of blocks which are diagonal. This fact plus unitarity leads to a single parameter α , a rotationlike angle characterizing the vectors $A_{L\lambda}$. This represents the coupling between the two Γ_8^+ representations (which are spin-orbit diagonal) by the V_4 potential term. Along with the phase shifts $\eta_{\Gamma_6^+}$, $\eta_{\Gamma_6^-}$, $\eta_{\Gamma_8^-}$, $\eta_{\Gamma_8^+}$, $\eta_{\Gamma_7^+}$, and $\eta_{\Gamma_8^+}$ associated with the irreducible representations, the inclusion of this parameter α leads to a total of seven quantities required to relativistically parametrize the Fermi surface with $l^{\max} = 2$. The explicit form of the matrices \bar{A}' and \bar{R} is given in the Appendix.

When non-muffin-tin effects are included, the least-squares-fit procedures discussed in the introduction must be modified slightly. In addition to derivatives of the areas with respect to the irreducible representation phase shifts, one must also calculate the derivative of the areas with respect to the rotation angle α ; i. e., we require $\partial \bar{M} / \partial \eta$ and $\partial \bar{M} / \partial \alpha$. The number of matrix element de-

derivatives which must be computed is smaller if we rewrite Eq. (13) in the form

$$\vec{M} = \vec{R}^t \cdot \vec{B} \cdot \vec{R} + E^{1/2} \vec{A}' \cdot \vec{C} \cdot \vec{A}^t \quad (16a)$$

and

$$C_{\lambda\lambda'} = \delta_{\lambda\lambda'} \cot \eta_{\lambda}. \quad (16b)$$

This is the form actually implemented.

IV. APPLICATION TO MOLYBDENUM AND TUNGSTEN

The procedures discussed in Sec. III were applied to the body-centered-cubic transition metals, molybdenum and tungsten. Studies of the dHvA effect have been carried out by a number of workers,²⁴⁻³⁰ but the most complete data are those of Hoekstra and Stanford²⁸ (HS) for Mo and Girvan, Gold, and Phillips³⁰ (GGP) for W. A great deal of work has also been done on the band structure of

these materials. Lomer³¹ was the first to propose a model for the Fermi surface of the chromium group metals based on the APW energy bands of iron calculated by Wood.³² Nonrelativistic APW band structure calculations have appeared for Mo (Ref. 33) and W (Refs. 33 and 34); relativistic APW calculations have been performed by Loucks³⁵ for W and by Koelling, Mueller, Ketterson, and Arko³⁶ and Christensen³⁷ for Mo. Iverson and Hodges³⁸ generated a band structure for Mo by fitting a nonrelativistic APW calculation to the Slater-Koster interpolation scheme; the effect of spin orbit coupling was included as a parameter. Figure 1 shows the Fermi surface of tungsten together with various external areas and their designated Greek letters. Cross sections of the surface, resulting from the present work, in the (100) and (110) planes are shown in Fig. 2 for Mo and Fig. 3 for W. The

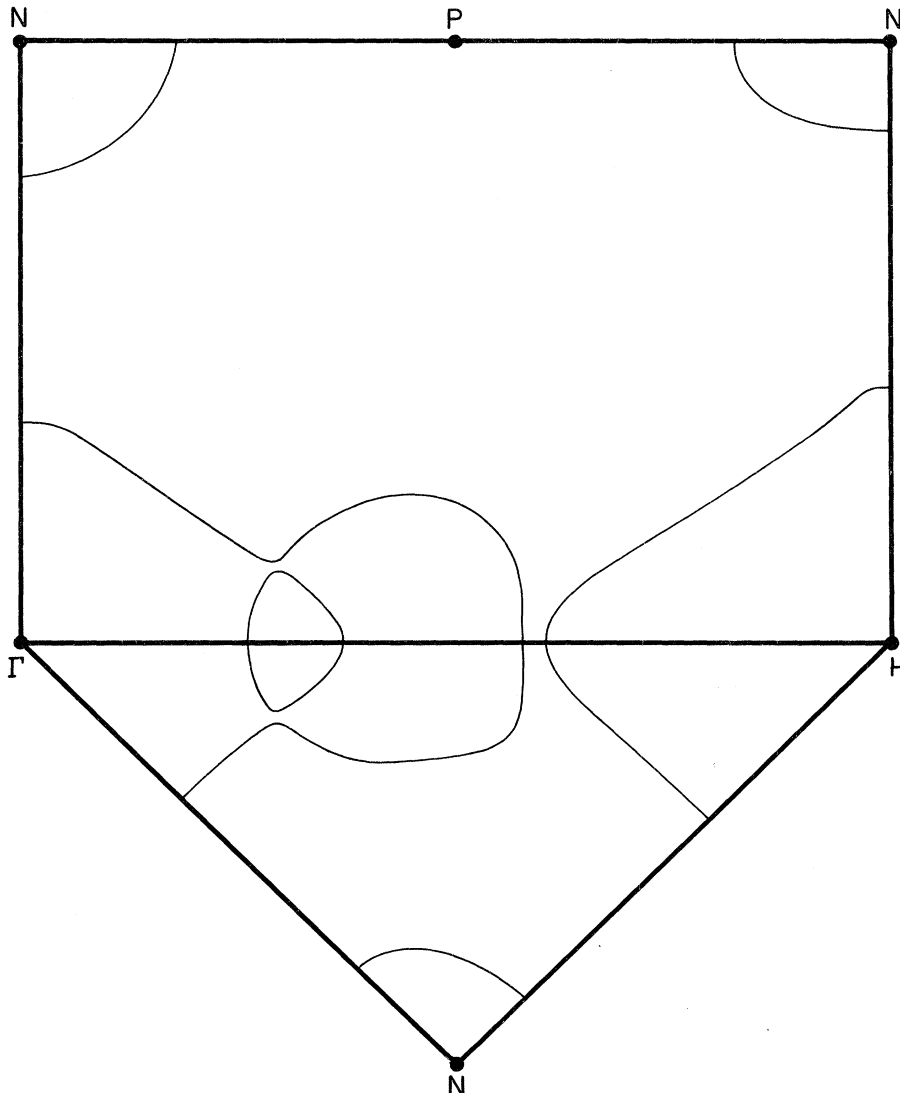


FIG. 2. Cross sections of the Fermi surface of Mo in the (100) and (110) planes resulting from our non-spherical-muffin-tin phase-shift fit to the dHvA data of Hoekstra and Stanford.

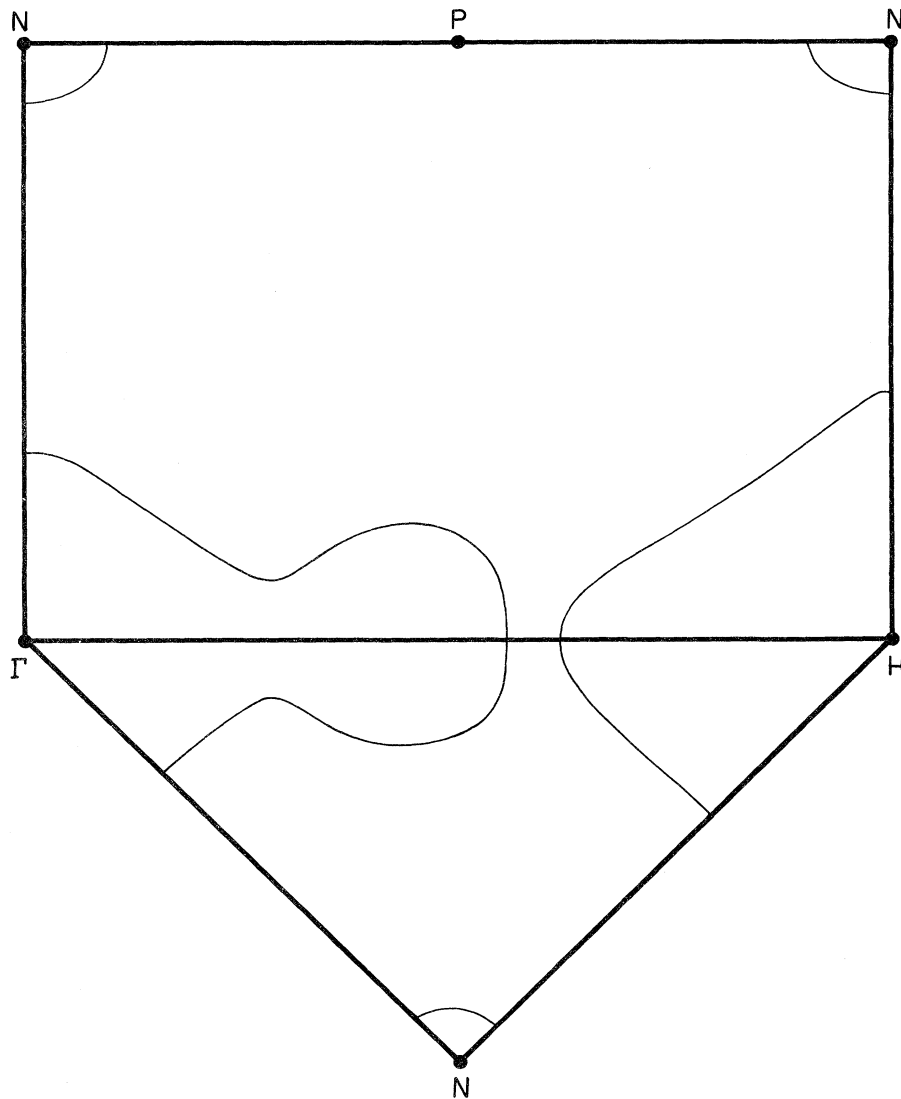


FIG. 3. Cross sections of the Fermi surface of W in the (100) and (110) planes resulting from our non-spherical-muffin-tin phase-shift fit to the dHvA data of Girvan, Gold, and Phillips.

large electron surface centered at Γ is referred to as the jack. The large hole sheet at H is called the octahedron. Finally, there is a small hole ellipsoid at the point N . Since Mo and W have an even atomic number the total volume of the hole surfaces must equal that of the electron surfaces.

The least-squares-fit procedure outlined above is a linearization of a basically nonlinear problem. Thus we must have an initial set of phase shifts from which to start our iterations. The initial phase shifts were calculated from the logarithmic derivatives computed by numerically integrating the radial Schrödinger equation; an overlapping atomic charge density model with full Slater exchange was used to construct the potential. In units of $(2\pi/a)^2$ the Fermi energy used was 0.67543 and 0.77020 for Mo and W, respectively. In Bohr radii (a.u.), the lattice constants used were 5.9468 and 5.9810 for Mo and W,

respectively; these are room-temperature values used by Loucks³⁵ but the correction on going to helium temperatures is smaller than the estimated experimental accuracy of the dHvA data. The Fermi energy in W was chosen to be the same as the relativistic APW calculations of Loucks³⁵; the energy in Mo was determined from the work of Koelling *et al.*³⁶ In any event the quality of fit has been found to be very insensitive to the Fermi energy parameter selected. This is consistent with the observation that the only real effect of the variation of the energy parameter is to find that energy for which the $l = L_{\max} + 1 = 3$ phase shift is zero (of course all the phase shifts with $l \leq L_{\max}$ readjust for each value of the energy parameter^{8,39}). In fact, for those formalisms which would eliminate the interstitial region,⁶ the Fermi energy parameter becomes little more than a convergence parameter⁴⁰

TABLE I. Comparison of areas calculated using the parameters of Table II to the experimental values obtained from de Haas-van Alphen data.

Surface, orbit, section	Field coordinate θ ($\varphi = 45^\circ$)	Orbit center ($2\pi/a$)			Experimental area ($2\pi/a$) ²	Calculated area ($2\pi/a$) ²	Error (%)
Molybdenum							
jack τ	0.0	0.0	0.0	0.0	0.5531	0.5487	0.80
jack ξ	54.7	0.0	0.0	0.0	0.2028	0.2048	-0.99
jack φ	90.0	0.0	0.0	0.0	0.3783	0.3774	0.24
jack π	0.0	0.0	0.0	0.4403	0.07578	0.07713	-1.78
jack σ	0.0	0.0	0.0	0.2896	0.02808	0.02836	-1.00
lense β	90.0	0.0	0.0	0.3	0.01225	0.01216	0.73
octahedron ν_1	0.0	0.0	0.0	1.0	0.3604	0.3608	-0.11
octahedron ν_2	54.7	0.0	0.0	1.0	0.2479	0.2516	-1.49
octahedron ν_3	90.0	0.0	0.0	1.0	0.2715	0.2734	-0.70
ellipsoid ρ_1 <i>NTH</i>	0.0	0.5	0.5	0.0	0.05435	0.05426	0.17
ellipsoid ρ_2 <i>NPH</i>	90.0	0.5	0.5	0.0	0.06297	0.06319	-0.35
ellipsoid ρ_3 <i>NPT</i>	90.0	-0.5	0.5	0.0	0.08728	0.08695	0.38
Tungsten							
jack τ	0.0	0.0	0.0	0.0	0.4320	0.4327	-0.16
jack ξ	54.7	0.0	0.0	0.0	0.1545	0.1544	0.06
jack φ	90.0	0.0	0.0	0.0	0.2916	0.2912	0.14
jack π	0.0	0.0	0.0	0.4424	0.05283	0.05286	-0.06
jack σ	0.0	0.0	0.0	0.2874	0.01483	0.01480	0.20
octahedron ν_1	0.0	0.0	0.0	1.0	0.3476	0.3460	0.46
octahedron ν_2	54.7	0.0	0.0	1.0	0.2393	0.2402	-0.38
octahedron ν_3	90.0	0.0	0.0	1.0	0.2589	0.2598	-0.35
ellipsoid ρ_1 <i>NTH</i>	0.0	0.5	0.5	0.5	0.01436	0.01437	-0.06
ellipsoid ρ_2 <i>NPH</i>	90.0	0.5	0.5	0.0	0.01945	0.01948	-0.15
ellipsoid ρ_3 <i>NPT</i>	90.0	-0.5	0.5	0.0	0.02233	0.02227	0.27

or, at most, a parameter fixing the curvature (kinetic energy) of the basis functions in the interstitial region.⁴¹

In selecting the experimental areas to include in a least-squares fit involving the phase shift parameters, one desires orbits which sample the surface in some favorable way. It is not possible *a priori* to define an optimal set, but we have selected orbits which include the extremities of the various surfaces. For these orbits and magnetic field usually lies along a symmetry direction and the angular derivatives of the frequency vanish thus making the data less sensitive to a crystal misalignment. After a fit is completed, the phase shift derivatives give a measure of the sensitivity of a given extremal area to a change in a phase shift. Table I lists the experimental areas used in the fit together with the calculated area resulting from the converged fit;

TABLE II. Values of the nonspherical muffin-tin parameters.

	Molybdenum	Tungsten
$\eta_{\Gamma_6^+}$	-0.74213	-0.69715
$\eta_{\Gamma_6^-}$	-0.31580	-0.37692
$\eta_{\Gamma_8^-}$	-0.30073	-0.35301
$\eta_{\Gamma_8^+}(3/2)$	-1.1072	-1.1929
$\eta_{\Gamma_8^+}(5/2)$	-1.3184	-1.6835
$\eta_{\Gamma_8^+}(5/2)$	-1.2791	-1.6962
α	0.42863	0.16333
rms error	0.885%	0.245%

shown also are the polar coordinates of the magnetic field directions and the coordinates of the orbit centers. The computation of the nine fitted areas associated with a given iteration for tungsten required approximately $1\frac{1}{2}$ min on an IBM 360-195 computer. The steps along the orbits were approximately $2\frac{1}{2}^\circ$ and the minimum amount of area required by symmetry was swept out. The W calculations were carried to a somewhat higher level of convergence. As pointed out by GGP it is not possible to distinguish from dHvA cross-sectional-area measurements whether the shortest semiaxis of the ellipsoid is along *NH* or *NT*. Since the band-structure calculations yield the result that the *NH* axis is smallest we assign our frequencies to conform with this conclusion as did GGP. For both Mo and W approximately five iterations were required to obtain convergence. The values of the converged phase shifts (in radians) are listed in Table II. The root-mean-square error was 0.89% for molybdenum and 0.24% for tungsten. In order to check how well our model is working for areas which are not included in the fit, we calculated, at 5° intervals, the extremal areas of the hole octahedron in the (110) plane. The rms deviation between the calculated and experimental area was 0.34% for W.

The orbit selection used for Mo and W introduced an additional complication. The σ and π orbits are not centered on a point having inversion symmetry and thus both the location and area of the extremal orbit must be computed. The program computes

both $A(k_{||})$ and $\partial A(k_{||})/\partial k_{||}$ for a given orbit so if these quantities are calculated for two orbits (labeled 1 and 2) in the vicinity of the extremum, the location and the value of the extremal area can be computed from

$$k_{||}^{\text{ext}} = \left(k_2 \frac{\partial A_1}{\partial k} - k_1 \frac{\partial A_2}{\partial k} \right) / \left(\frac{\partial A_1}{\partial k} - \frac{\partial A_2}{\partial k} \right), \quad (17a)$$

$$A(k_{||}^{\text{ext}}) = A_1 + \frac{\partial A_1}{\partial k} (k_{||}^{\text{ext}} - k_1), \quad (17b)$$

$$\frac{\partial^2 A}{\partial k_{||}^2} = \left(\frac{\partial A_1}{\partial k} - \frac{\partial A_2}{\partial k} \right) / (k_1 - k_2). \quad (17c)$$

For a given iteration the position of the extremum ($k_{||}^{\text{ext}}$) was computed; on the succeeding iteration the computations for one of the orbits were made at the value of $k_{||}^{\text{ext}}$ for the preceding iteration and these results were included in the least-squares fit. As the calculation converges the value of $k_{||}^{\text{ext}}$ stabilizes. The calculations for the neighboring orbit were not fitted. This procedure was necessary because the position of the extremum was observed to shift somewhat as the iterations proceeded; especially for the σ orbit.

In addition to using an optimal set of orbits, it would be desirable to include the requirement of volume compensation. This would be one additional "datum point" obtained without further measurements. This additional information, however, is quite expensive both in terms of additional computational time and of additional effort required to design the integration technique. For this reason, we have not included volume compensation in our present calculation.

The derivatives of the areas with respect to the phase shifts and the rotation angle are shown in Table III; listed also is the "structure constant mass" $(\partial A/\partial E)_{\vec{\eta}}$. These quantities can be used to invert cyclotron effective mass data to obtain Fermi velocities⁸ (under the assumption that the electron phonon mass enhancement can be lumped into the energy dependence of the phase shifts). The cyclotron mass is given by

$$m^* = \frac{1}{\pi} \frac{\partial A}{\partial E} = \frac{1}{\pi} \left[\left(\frac{\partial A}{\partial E} \right)_{\vec{\eta}} + \left(\frac{\partial A}{\partial \vec{\eta}} \right)_E \cdot \vec{\eta}' \right], \quad (18)$$

where the $\vec{\eta}' = \partial \vec{\eta}/\partial E$ are new set of parameters. The Fermi velocity is then given by

$$\frac{\partial E}{\partial \vec{k}} = - \left(\frac{\partial \lambda^{(\vec{n})}}{\partial \vec{k}} \right)_E / \left(\frac{\partial \lambda^{(\vec{n})}}{\partial E} \right)_{\vec{k}}, \quad (19a)$$

where

$$\left(\frac{\partial \lambda^{(\vec{n})}}{\partial E} \right)_{\vec{k}} = \left(\frac{\partial \lambda^{(\vec{n})}}{\partial E} \right)_{\vec{k}, \vec{\eta}} + \left(\frac{\partial \lambda^{(\vec{n})}}{\partial \vec{\eta}} \right)_{\vec{k}, E} \cdot \vec{\eta}'. \quad (19b)$$

For the nonrelativistic case, Coleridge⁴² has shown how the area phase-shift derivatives may be used to invert the dHvA orbitally averaged scattering lifetimes into local lifetimes by introducing a new set of parameters; a relativistic nonspherical muffin-tin generalization of this theory (which has yet to be worked out) might also make use of the information in Table III. The data in Tables II and III are given to five figures; these are not all significant (perhaps three of them are) and the extra digits are carried to enable a consistent comparison between these and other calculations.

TABLE III. Area phase-shift derivatives.

	A_τ	A_t	A_σ	A_π	A_σ	A_β	A_{ν_1}	A_{ν_2}	A_{ν_3}	A_{ρ_1}	A_{ρ_2}	A_{ρ_3}
Molybdenum												
$\partial A/\partial \eta_{\Gamma_4^+}$	0.01076	0.00322	0.00419	0.00190	0.00053	0.00009	-0.00358	-0.03524	-0.03759	-0.04186	-0.00005	-0.06285
$\partial A/\partial \eta_{\Gamma_4^-}$	0.19470	0.02157	0.08021	0.04738	0.00615	0.00134	-0.18498	-0.07583	-0.11033	-0.18935	-0.24133	-0.32092
$\partial A/\partial \eta_{\Gamma_5^-}$	0.51293	0.06699	0.22231	0.07931	0.01905	0.00507	-0.14302	-0.09925	-0.11307	-0.37118	-0.46190	-0.61502
$\partial A/\partial \eta_{\Gamma_5^+(\delta/2)}$	0.64650	0.22606	0.40093	0.12995	0.09549	0.03600	-0.40427	-0.20630	-0.25584	-0.00594	-0.02456	-0.03336
$\partial A/\partial \eta_{\Gamma_5^-}$	0.38905	0.17211	0.26189	0.06129	0.04758	0.03633	-0.04646	-0.05235	-0.04925	-0.00040	-0.01055	-0.01577
$\partial A/\partial \eta_{\Gamma_5^+(\delta/2)}$	0.30891	0.01539	0.18123	0.11237	0.05334	0.04416	-0.01911	-0.01223	-0.01601	-0.04989	-0.04362	-0.01582
$\partial A/\partial \alpha$	0.04932	0.01962	0.02866	0.00612	0.00357	0.00158	-0.02916	-0.01557	-0.01984	0.00508	0.00250	-0.00119
$\partial A/\partial E$	1.0500	0.24809	0.59614	0.23105	0.12333	0.07276	-0.39701	-0.25297	-0.29840	-0.28434	-0.32026	-0.44449
Tungsten												
$\partial A/\partial \eta_{\Gamma_4^+}$	0.00546	0.00070	0.00304	0.00218	0.00011	...	-0.03113	-0.05790	-0.05604	-0.00940	-0.00024	-0.01453
$\partial A/\partial \eta_{\Gamma_4^-}$	0.12501	0.00850	0.05907	0.03560	0.00052	...	-0.28185	-0.12187	-0.16036	-0.20574	-0.28642	-0.32350
$\partial A/\partial \eta_{\Gamma_5^-}$	0.44519	0.06769	0.25162	0.07780	0.02491	...	-0.08218	-0.07699	-0.08575	-0.40274	-0.55339	-0.62798
$\partial A/\partial \eta_{\Gamma_5^+(\delta/2)}$	0.46189	0.14524	0.29252	0.08540	0.04871	...	-0.37348	-0.17911	-0.21458	-0.00546	-0.00987	-0.00956
$\partial A/\partial \eta_{\Gamma_5^-}$	0.61412	0.31843	0.44639	0.07337	0.09711	...	-0.01325	-0.02878	-0.02866	-0.00008	-0.00378	-0.00442
$\partial A/\partial \eta_{\Gamma_5^+(\delta/2)}$	0.33438	0.01960	0.18904	0.09968	0.02292	...	-0.07649	-0.04758	-0.05508	-0.00935	-0.00995	-0.00468
$\partial A/\partial \alpha$	0.13250	0.05009	0.08333	0.01971	-0.01783	...	-0.15772	-0.08416	-0.10013	0.00599	0.00393	-0.00011
$\partial A/\partial E$	0.97360	0.24244	0.58764	0.18856	0.09681	...	-0.41431	-0.25877	-0.29964	-0.26223	-0.35363	-0.40516

TABLE IV. Extremal dimensions of the Mo and W Fermi surface ($2\pi/a$).

Surface	Dimension	Present work	HS ^a Inversion	RFSE	GR
Molybdenum ^b					
jack	Γ toward H	0.5733	...	0.58 ^c 0.55 ^e	0.60 ^d
jack	Γ toward P	0.2355	...	0.235 ^c 0.22 ^e	...
jack	Γ toward N	0.2602	...	0.26 ^c	...
jack	$\frac{1}{2}$ neck caliper \perp to Δ in (100) plane	0.0971	...	0.095 ^c	...
jack	$\frac{1}{2}$ neck caliper \perp to Δ in (110) plane	0.0930
jack	$\frac{1}{2}$ ball caliper \perp to Δ in (100) plane	0.1446	0.15 ^d
jack	$\frac{1}{2}$ ball caliper \perp to Δ in (110) plane	0.1695	...	0.175 ^c 0.17 ^e	0.17 ^d
Octahedron	H toward Γ	0.3954	0.407	0.395 ^c 0.376 ^e	...
Octahedron	H toward P	0.2524	0.244	0.255 ^c 0.238 ^e	...
Octahedron	H toward N	0.3002	0.304	0.30 ^c 0.290 ^e	0.30 ^d
Lense	$\frac{1}{2}$ of caliper \perp to Δ in (110) plane	0.0818	...	0.078 ^c 0.060 ^e	...
Lense	$\frac{1}{2}$ of caliper along Δ	0.0548
Ellipsoid	N toward P	0.1808	0.183	0.19 ^c	0.14 ^c
Ellipsoid	N toward Γ	0.1624	0.163	0.15 ^c 0.16 ^e	...
Ellipsoid	N toward H	0.1084	0.108	0.11 ^c 0.10	0.105 ^f
Tungsten ^j					
Surface	Dimension	Present work	GGP ^g Inversion	RFSE	GR ⁱ
jack	Γ toward H	0.5552	0.5527	0.559	0.523
jack	Γ toward P	0.2063	0.202	0.209	...
jack	Γ toward N	0.2243	0.239
jack	$\frac{1}{2}$ neck caliper \perp to Δ in (100) plane	0.0691	0.0738
jack	$\frac{1}{2}$ neck caliper \perp to Δ in (110) plane	0.0682	0.0662
jack	$\frac{1}{2}$ ball caliper \perp to Δ in (100) plane	0.1234	0.121	...	0.121
jack	$\frac{1}{2}$ ball caliper \perp to Δ in (110) plane	0.1363	0.135	...	0.126
Octahedron	H toward Γ	0.3848	0.3826	0.39	0.35
Octahedron	H toward P	0.2450	0.2413	0.25	...
Octahedron	H toward N	0.2955	0.2937	0.30	0.297
Ellipsoid	N toward P	0.0627	0.0629
Ellipsoid	N toward Γ	0.0734	0.0723
Ellipsoid	N toward H	0.0982	0.0978

^aHoekstra and Stanford (Ref. 28).^bFor molybdenum, to obtain data in \AA^{-1} multiply the entries in this table by 1.9966.^cBoiko *et al.* (Ref. 43).^dJones and Rayne (Ref. 47).^eCleveland and Stanford (Ref. 44).^fBezuglyi *et al.* (Ref. 48).^gGirvan, Gold, and Phillips (Ref. 30).^hWalsh and Grimes (Ref. 46).ⁱJones and Rayne (Ref. 47).^jFor tungsten, to obtain data in \AA^{-1} multiply the entries in this table by 1.9853.

Table IV contains the Fermi radii along symmetry directions for the jack, octahedron, and ellipsoid. Some of these have been observed directly in Gantmakher radio-frequency size effect⁴³⁻⁴⁶ (RFSE) and magnetoacoustic geometric-resonance^{47,48} (GR) experiments; the measured values are also included in Table IV. In both of these types of experiments one measures caliper dimension of the Fermi surface in a direction mutually perpendicular to the field direction \hat{H} and a second direction \hat{q} ; \hat{q} is the propagation direction for the magnetoacoustic measurements while it is the direction of the normal to the parallel sample faces in the Gantmaker experiments. Table IV contains additional caliper radii on the jack which one would observe for $\hat{H} \parallel [100]$ and $\hat{q} \parallel [010]$ and $[011]$; for each of these \hat{q} directions the caliper radii are associated with the ball and the neck of the jack. Two lens dimensions in Mo are also listed.

V. DISCUSSION AND CONCLUSIONS

Various algebraic models have been used to represent the sheets of the Mo and W Fermi Surface and to invert the dHvA data. GGP used an implicit equation for the octahedron; this has the disadvantage that it requires an iterative solution but the advantage that a very good representation was achieved with three parameters. The Mueller inversion scheme^{49,50} has been applied to the hole octahedron by HS; more parameters (11) were required with this technique but the calculations are much more straightforward. A problem which occurs in the application of the Mueller scheme to highly nonspherical surfaces (like the octahedron) is that spurious "oscillations" tend to occur in the resulting radii. If data are collected in additional nonsymmetry planes these oscillations can be suppressed⁵¹; the inversions of HS do show some signs of these oscillations although the results are, on the whole, reasonable. It has been shown⁵² that the Mueller inversion scheme can be used to fit the differences between the areas deduced from an analytical model and the data; it is our opinion that using this procedure with the GGP model would result in a more accurate inversion than either technique separately could achieve. GGP constructed an eleven parameter algebraic model for the jack that gave a quite satisfactory representation of their data. The spherical mapping procedure of Ketterson and Windmiller⁵² was used by HS to invert the data on the ellipsoids. The results of these various inversions have also been included in Table IV.

The data of Table IV show quite convincingly that the dimensions resulting from our band structure based inversion of the dHvA data of Mo and W are quite consistent with other dHvA inversions as well as the more direct RFSE and GR measure-

ments. Using the nonspherical RKKR technique this has been accomplished for all sheets of the Fermi surface with only seven parameters. The near degeneracy of the Γ_7^+ ($\frac{5}{2}$) and Γ_8^+ ($\frac{5}{2}$) phase shifts suggests that nearly as good a fit could be accomplished by requiring these two quantities to be identical which would reduce the total number of parameters by one. The inversion by GGP, which was on the whole rather economical in its use of adjustable constants, required a total of 17 parameters to accomplish the same goal (three each for the ellipsoid and octahedron and eleven for the jack). The principal advantage being suggested here for the phase shift parameterization technique is not just that it uses a minimum number of parameters but that it places constraints on the data and so provides checks on the interpretation of that data and the adequacy of the fitting procedure. This feature is nicely illustrated by the failure of the muffin-tin model. Otherwise, the simple mathematical representations are easier to code and faster to generate but place no bounds on the data to be represented other than the inventiveness of the fitter. Such conveniences would easily repay the necessity of using the extra parameters. Because the mathematical representations place no restrictions, one only has as much information in the fit as was available initially. On the other hand, the RKKR fits should be capable of extrapolations to other experiments. Thus, in addition to the extremal areas and calipers observed in dHvA and RFSE or GR measurements used in the fitting, the inflection and limiting point resonances which occur in the magnetomorphic size effect⁵³ and Doppler-shifted-cyclotron-resonance experiments⁵⁴ would be interesting to calculate; this will be the subject of a future investigation.

The over-all rms error we have achieved is consistent with the estimated error of the experiments. It would be very desirable to obtain more accurate measurements of the principal dHvA frequencies along symmetry directions using *in situ* NMR calibration and precise sample orientation as have been done in noble metals⁵⁵; such data would provide a more challenging test of the RKKR inversion technique described here. Indeed in our previous work on noble metals the rms error was quite sensitive to the quality of the data, the better NMR calibrated data allowing the superior fit.

As mentioned above, one would expect the non-muffin-tin correction to be most significant in those regions of the Brillouin zone far from symmetry points, lines, and planes. This is because there is no symmetry selection operating in these regions. At the high-symmetry points, the transformation properties of the wave functions often dictate that a state will have a pure l character or

very limited mixture. (Γ_8^+ is pure d in our model, for example.) Then the only effect of the non-muffin-tin correction is to spread slightly the eigenvalues (the two Γ_8^+ states, for example). However, when one is investigating a general point away from a symmetry point, these limitations no longer exist and one will in general get hybridizing s , p , and d components. Then as one shifts the different d -components relative to each other (the only direct effect of the additional potential interaction), their interaction with the s and p components will change dramatically. It is through this indirect effect on hybridization that the major changes occur. Thus, those orbits passing through the center of the $\frac{1}{48}$ th wedge where the most hybridization occurs will be the most sensitive to the non-muffin-tin corrections. The π orbit on the jack is a prime example. Thus all information about the knobs of the electron jack is particularly useful.

The importance of the relativistic effects is most apparent from examining the dimensions of the lens and the jack neck; these two surfaces actually make contact in a nonrelativistic formalism. For tungsten, where relativistic effects are most important, the lens surface is nonexistent. For molybdenum the splitting between the semicalipers perpendicular to Δ is approximately $0.011 2\pi/a$ units.

The accuracy which can be achieved with dHvA measurements, in general, exceeds that of other Fermi surface probing techniques such as the RFSE or GR. The drawback of the dHvA effect has been that it measures extremal areas rather than dimensions. It is our opinion that with the availability of accurate inversion techniques of the type discussed in this paper, the dHvA effect should continue to be the favored experimental technique for future Fermi-surface investigations.

ACKNOWLEDGMENTS

We wish to thank G. W. Crabtree and F. M. Mueller for helpful discussions; T. M. Kirkman for his assistance with the reentrant Fermi-surface problem; and the Computer Center of the Applied Mathematics Division, Argonne National Laboratory for excellent service.

APPENDIX

For the nonrelativistic case with $l^{\max} = 2$ the R matrix is a unit matrix except in the d block where it acts to construct the E_g and T_{2g} states from the spherical harmonics. The state Y_{20} is a member of the E_g set; also, Y_{21} $Y_{2\bar{1}}$ belong to the T_{2g} set. The remaining E_g and T_{2g} states are $(1/\sqrt{2})(Y_{22} + Y_{2\bar{2}})$ and $(1/\sqrt{2})(Y_{22} - Y_{2\bar{2}})$, respectively. Thus the \mathbf{R} matrix in the d block has the form

TABLE V. d states in the angular-momentum representation.

$j = \frac{3}{2} (\kappa = 2)$	$j = \frac{5}{2} (\kappa = -3)$
$ \frac{3}{2}, \frac{3}{2}\rangle = \begin{bmatrix} -1/\sqrt{5} & Y_{21} \\ \sqrt{4/5} & Y_{2\bar{2}} \end{bmatrix}$	$ \frac{5}{2}, \frac{5}{2}\rangle = \begin{bmatrix} Y_{22} \\ 0 \end{bmatrix}$
$ \frac{3}{2}, -\frac{3}{2}\rangle = \begin{bmatrix} -\sqrt{4/5} & Y_{2\bar{2}} \\ 1/\sqrt{5} & Y_{2\bar{1}} \end{bmatrix}$	$ \frac{5}{2}, -\frac{5}{2}\rangle = \begin{bmatrix} 0 \\ Y_{22} \end{bmatrix}$
$ \frac{3}{2}, \frac{1}{2}\rangle = \begin{bmatrix} -\sqrt{2/5} & Y_{20} \\ \sqrt{3/5} & Y_{21} \end{bmatrix}$	$ \frac{5}{2}, \frac{3}{2}\rangle = \begin{bmatrix} \sqrt{4/5} & Y_{21} \\ 1/\sqrt{5} & Y_{22} \end{bmatrix}$
$ \frac{3}{2}, -\frac{1}{2}\rangle = \begin{bmatrix} -\sqrt{3/5} & Y_{2\bar{1}} \\ \sqrt{2/5} & Y_{20} \end{bmatrix}$	$ \frac{5}{2}, -\frac{3}{2}\rangle = \begin{bmatrix} 1/\sqrt{5} & Y_{2\bar{2}} \\ \sqrt{4/5} & Y_{2\bar{1}} \end{bmatrix}$
	$ \frac{5}{2}, \frac{1}{2}\rangle = \begin{bmatrix} \sqrt{3/5} & Y_{20} \\ \sqrt{2/5} & Y_{21} \end{bmatrix}$
	$ \frac{5}{2}, -\frac{1}{2}\rangle = \begin{bmatrix} \sqrt{2/5} & Y_{2\bar{1}} \\ \sqrt{3/5} & Y_{20} \end{bmatrix}$

$$\begin{bmatrix} |T_{2g} 1\rangle \\ |T_{2g} 2\rangle \\ |T_{2g} 3\rangle \\ |E_g 1\rangle \\ |E_g 2\rangle \end{bmatrix} = \begin{bmatrix} 0 & 0 & 1 & 0 & 0 \\ 0 & 0 & 0 & 1 & 0 \\ \frac{1}{\sqrt{2}} & -\frac{1}{\sqrt{2}} & 0 & 0 & 0 \\ \frac{1}{\sqrt{2}} & \frac{1}{\sqrt{2}} & 0 & 0 & 0 \\ 0 & 0 & 0 & 0 & 1 \end{bmatrix} \begin{bmatrix} Y_{22} \\ Y_{2\bar{2}} \\ Y_{21} \\ Y_{2\bar{1}} \\ Y_{20} \end{bmatrix}, \quad (\text{A1})$$

The relativistic secular equation for the spherical muffin-tin case is usually written in the angular momentum representation; Table V lists the d states in the angular momentum representation. The $d_{3/2}$ states transform as Γ_8^+ and thus require no modification. The $d_{5/2}$ states are a mixture of Γ_7^+ and Γ_8^+ . We require a similarity transformation which acts on the $d_{5/2}$ states to produce the separated Γ_7^+ and Γ_8^+ states; we further require that the resulting Γ_8^+ representation be identical to the Γ_8^+ representation of $d_{3/2}$ states.

Parada⁵⁶ has used a set of wave functions for the T_{2g} states which are diagonal in the V_4 terms in the potential (the crystal field representation); these states are listed in Table VI. Using Tables V and VI we easily verify that the Γ_7^+ states of Parada are given by

$$|\Gamma_7^+ 1\rangle = (1/\sqrt{6}) \left| \frac{5}{2}, \frac{5}{2} \right\rangle - \sqrt{\frac{5}{6}} \left| \frac{5}{2}, -\frac{3}{2} \right\rangle, \quad (\text{A2a})$$

TABLE VI. d states in the crystal-field representation.

E_g	T_{2g}
$ \Gamma_8^+ a1\rangle = \frac{1}{\sqrt{2}} \begin{bmatrix} 0 \\ -Y_{22} - Y_{2\bar{2}} \end{bmatrix}$	$ \Gamma_8^+ b1\rangle = \frac{1}{\sqrt{3}} \begin{bmatrix} -Y_{21} \\ Y_{22} - Y_{2\bar{2}} \end{bmatrix}$
$ \Gamma_8^+ a2\rangle = \begin{bmatrix} Y_{20} \\ 0 \end{bmatrix}$	$ \Gamma_8^+ b2\rangle = \begin{bmatrix} 0 \\ Y_{21} \end{bmatrix}$
$ \Gamma_8^+ a3\rangle = \begin{bmatrix} 0 \\ -Y_{20} \end{bmatrix}$	$ \Gamma_8^+ b3\rangle = \begin{bmatrix} -Y_{2\bar{1}} \\ 0 \end{bmatrix}$
$ \Gamma_8^+ a4\rangle = \frac{1}{\sqrt{2}} \begin{bmatrix} Y_{22} + Y_{2\bar{2}} \\ 0 \end{bmatrix}$	$ \Gamma_8^+ b4\rangle = \frac{1}{\sqrt{3}} \begin{bmatrix} Y_{22} - Y_{2\bar{2}} \\ Y_{2\bar{1}} \end{bmatrix}$
	$ \Gamma_7^+ 1\rangle = \frac{1}{\sqrt{6}} \begin{bmatrix} Y_{22} - Y_{2\bar{2}} \\ -2Y_{2\bar{1}} \end{bmatrix}$
	$ \Gamma_7^+ 2\rangle = \frac{1}{\sqrt{6}} \begin{bmatrix} -2Y_{21} \\ Y_{2\bar{2}} - Y_{22} \end{bmatrix}$

$$|\Gamma_7^+ 2\rangle = (1/\sqrt{6}) \left| \frac{5}{2}, -\frac{5}{2} \right\rangle - \sqrt{\frac{3}{6}} \left| \frac{5}{2}, \frac{3}{2} \right\rangle. \quad (\text{A2b})$$

From the condition of unitarity we obtain two of the states of a Γ_8^+ representation; the remaining two Γ_8^+ states are formed from the $|\frac{5}{2}, \frac{1}{2}\rangle$ and $|\frac{5}{2}, -\frac{1}{2}\rangle$ states. We write the states of our Γ_8^+ representation in the form

$$|\Gamma_8^+ \frac{5}{2}, \frac{3}{2}\rangle = -\sqrt{\frac{5}{6}} \left| \frac{5}{2}, -\frac{5}{2} \right\rangle - (1/\sqrt{6}) \left| \frac{5}{2}, \frac{3}{2} \right\rangle, \quad (\text{A3a})$$

$$|\Gamma_8^+ \frac{5}{2}, -\frac{3}{2}\rangle = \sqrt{\frac{5}{6}} \left| \frac{5}{2}, \frac{5}{2} \right\rangle + (1/\sqrt{6}) \left| \frac{5}{2}, -\frac{3}{2} \right\rangle, \quad (\text{A3b})$$

$$|\Gamma_8^+ \frac{5}{2}, \frac{1}{2}\rangle = \left| \frac{5}{2}, \frac{1}{2} \right\rangle, \quad (\text{A3c})$$

$$|\Gamma_8^+ \frac{5}{2}, -\frac{1}{2}\rangle = -\left| \frac{5}{2}, -\frac{1}{2} \right\rangle. \quad (\text{A3d})$$

The particular choice of sign in Eqs. (A3a) and (A3d) was selected so that the states of this representation transform identically like the states of the $j = \frac{3}{2}$ angular momentum Γ_8^+ representation. This was verified by observing that the states of the T_{2g} Γ_8^+ representation of Parada can be written as a linear combination states $|\Gamma_8^+, \frac{5}{2}, i\rangle$ and $|\frac{3}{2}, i\rangle$; i. e.,

$$|\Gamma_8^+ b, i\rangle = \sqrt{\frac{2}{5}} |\Gamma_8^+, \frac{5}{2}, i\rangle + \sqrt{\frac{3}{5}} \left| \frac{3}{2}, i \right\rangle \quad (\text{A4a})$$

for all four values of i . From unitarity we derive the E_g states of the crystal-field representation listed in Table VI,

$$|\Gamma_8^+ a, i\rangle = \sqrt{\frac{3}{5}} |\Gamma_8^+, \frac{5}{2}, i\rangle - \sqrt{\frac{2}{5}} \left| \frac{3}{2}, i \right\rangle.$$

Thus our R matrix is a unit matrix except in the $j = \frac{5}{2}$ block where, from Eqs. (A2) and (A3), it has the form

$$R = \frac{1}{\sqrt{6}} \begin{bmatrix} 1 & 0 & 0 & -\sqrt{5} \\ 0 & 1 & -\sqrt{5} & 0 \\ 0 & -\sqrt{5} & -1 & 0 \\ \sqrt{5} & 0 & 0 & 1 \end{bmatrix}. \quad (\text{A5})$$

In addition, one must make the sign change implied by Eq. (A3d). The A' matrix differs from a unit matrix only in those blocks which can couple the states of the two Γ_8^+ representations

$$A' = \begin{bmatrix} \cos\alpha & \sin\alpha \\ -\sin\alpha & \cos\alpha \end{bmatrix}. \quad (\text{A6})$$

(Each entry in this matrix should be multiplied by a 4×4 unit matrix and there should be a number of unit and null matrix blocks. These have been suppressed.)

From the previous discussion it is clear that if $\sin\alpha = \sqrt{\frac{3}{5}}$ ($\alpha \cong 0.8861$ rad) our representation is diagonal in the crystal-field representation; for $\alpha = 0$ it is, of course, diagonal in the angular momentum representations. For lighter elements, where spin-orbit coupling is smaller, we would expect larger values of α since the V_4 terms in the potential would then be the most significant perturbation; indeed we observe that α is much larger in Mo than it is in W. In the limits when the spin-orbit coupling or crystal-field effects vanish, the $\eta_{\Gamma_8^+(5/2)}$ and $\eta_{\Gamma_7^+(5/2)}$ phase shifts should be identical. This implies that the splitting of these quantities is a measure of the product of spin-orbit coupling and crystal-field effects and should thus be small for all values of α ; this conclusion is born out by the results of our fits to the Mo and W data. We could probably constrain this phase shift splitting to vanish with no significant increase in the rms error; this would result in only six parameters for an $l^{\max} = 2$ fit.

*Work performed under the auspices of the U. S. Atomic Energy Commission.

†Present address: IBM Thomas J. Watson Research Laboratory, Yorktown Heights, N. Y. 10598.

¹A. P. Cracknell and K. C. Wong, *The Fermi Surface*, (Clarendon, Oxford, 1973).

²M. L. Cohen and V. Heine, *Solid State Phys.* **24**, 37 (1970).

³B. Segall and F. J. Ham, *Methods Compt. Phys.* **8**, 251 (1968).

⁴J. C. Slater, *Phys. Rev.* **51**, 151 (1973); T. L. Loucks, *The Augmented Plane Wave Method* (Benjamin, New York, 1967).

⁵J. Koringa, *Physica (Utr.)* **13**, 392 (1947); W. Kohn and N. Rostoker, *Phys. Rev.* **94**, 1111 (1954).

⁶A. R. Williams and Jane van W. Morgan, *J. Phys. C*

- 5, L293 (1972); 7, 37 (1974).
- ⁷B. Bosacchi, J. B. Ketterson, and L. R. Windmiller, Phys. Rev. B 4, 1197 (1971); J. B. Ketterson, F. M. Mueller, and L. R. Windmiller, Phys. Rev. 186, 656 (1969).
- ⁸J. C. Shaw, J. B. Ketterson, and L. R. Windmiller, Phys. Rev. B 5, 3894 (1972).
- ⁹T. Kirkman (unpublished).
- ¹⁰M. J. G. Lee, Phys. Rev. 178, 953 (1969); 187, 901 (1969); Phys. Rev. Lett. 26, 501 (1971); J. F. Cooke, H. L. Davis, and R. F. Wood, *ibid.* 25, 28 (1970).
- ¹¹D. D. Koelling and A. J. Freeman, Phys. Rev. B 7, 4454 (1973).
- ¹²Y. Onodera and M. Okazaki, J. Phys. Soc. Jpn. 21, 1273 (1966).
- ¹³S. Takada, Prog. Theor. Phys. 36, 224 (1966).
- ¹⁴J. Treusch, Phys. Status Solidi 19, 603 (1967).
- ¹⁵U. Rössler, Solid State Commun. 5, 45 (1967).
- ¹⁶W. Rudge, Phys. Rev. 181, 1020 (1969); 181, 1024 (1969); P. DeCicco, *ibid.* 153, 931 (1967); L. Kleinman and R. Shurtleff, *ibid.* 188, 1111 (1969).
- ¹⁷D. D. Koelling, A. J. Freeman, and F. M. Mueller, Phys. Rev. B 1, 1318 (1970).
- ¹⁸H. Bross and K. H. Anthony, Phys. Status Solidi 22, 667 (1967); F. Belezny and M. J. Lawrence, J. Phys. C 1, 1288 (1968); A. R. Williams, Phys. Rev. B 1, 3417 (1970); M. A. Ball, J. Phys. C 5, L23 (1972).
- ¹⁹W. John, G. Lehmann, and P. Ziesche, Phys. Status Solidi B 53, 287 (1972).
- ²⁰G. S. Painter, J. S. Faulkner, and G. M. Stocks, Phys. Rev. B 9, 2448 (1974). The authors of this conclude the nonspherical terms are important for transition metals in the center of the series. These are the bcc transition metals. We believe that this is the most relevant parameter. Additional support for this view can be found in the necessity of using different "potentials"—actually phase shifts—for the $d\epsilon$ and $d\gamma$ states to obtain reasonable results for V and Cr as found by S. Wakoh and J. Yamashita, J. Phys. Soc. Jpn. 35, 1394 (1973). Although they ascribe this effect to different effective intra-atomic exchange, we believe it to be the effect of the nonspherical V_4 potential term.
- ²¹Yu. M. Demkov and V. S. Rudakov, Zh. Eksp. Teor. Fiz. 59, 2035 (1970) [Sov. Phys.-JETP 32, 1103 (1971)].
- ²²R. Knox and A. Gold, *Symmetry in the Solid State* (Benjamin, New York, 1964), p. 108.
- ²³R. L. Jacobs, Phys. Lett. A 33, 417 (1970).
- ²⁴G. B. Brandt and J. A. Rayne, Phys. Lett. 3, 148 (1962).
- ²⁵G. B. Brandt and J. A. Rayne, Phys. Rev. 132, 1945 (1963).
- ²⁶D. M. Sparlin and J. A. Marcus, Phys. Rev. 144, 484 (1966).
- ²⁷G. Leaver and A. Myers, Philos. Mag. 19, 465 (1969).
- ²⁸J. A. Hoekstra and J. L. Stanford, Phys. Rev. B 8, 1416 (1973).
- ²⁹R. F. Girvan, USAEC Report, 1966 (unpublished).
- ³⁰R. F. Girvan, A. V. Gold, and R. A. Phillips, J. Chem. Phys. Solids 29, 1485 (1968).
- ³¹W. M. Lomer, Proc. Phys. Soc. Lond. 80, 489 (1962).
- ³²J. H. Wood, Phys. Rev. 126, 517 (1962).
- ³³T. L. Loucks, Phys. Rev. 139, A1181 (1965).
- ³⁴L. F. Mattheiss, Phys. Rev. 139, A1893 (1965).
- ³⁵T. L. Loucks, Phys. Rev. 143, 506 (1966).
- ³⁶D. D. Koelling, F. M. Mueller, J. B. Ketterson, and A. J. Arko, Phys. Rev. B 10, 4889 (1974).
- ³⁷N. E. Christensen, *Computational Solid State Physics*, edited by F. Herman, N. W. Dalton, T. R. Koehler (Plenum, New York, 1972), p. 155.
- ³⁸R. J. Iverson and L. Hodges, Phys. Rev. B 8, 1429 (1973).
- ³⁹O. K. Andersen, Phys. Rev. Lett. 27, 1211 (1971).
- ⁴⁰O. K. Andersen (private communications).
- ⁴¹O. K. Andersen, Solid State Commun. 13, 133 (1973); O. K. Andersen and R. V. Kasowski, *ibid.* 11, 799 (1972).
- ⁴²P. T. Coleridge, Phys. Rev. B 7, 3508 (1973).
- ⁴³V. V. Boiko, V. A. Gasparov, and I. G. Gverdsiteli, Zh. Eksp. Teor. Fiz. 56, 489 (1969) [Sov. Phys.-JETP 29, 267 (1969)]; V. V. Boiko and V. A. Gasparov, *ibid.* 61, 1976 (1971) [*ibid.* 34, 1054 (1972)].
- ⁴⁴J. R. Cleveland and J. L. Stanford, Phys. Rev. B 4, 311 (1971).
- ⁴⁵W. M. Walsh, Jr., C. C. Grimes, G. Adams, and L. W. Rupp, in *Proceedings of the Ninth International Conference on Low Temperature Physics*, edited by J. G. Daunt, D. O. Edwards, F. J. Milford, and M. Yaqub (Plenum, New York, 1965), p. 765.
- ⁴⁶W. M. Walsh, Jr., and C. C. Grimes, Phys. Rev. Lett. 13, 523 (1964).
- ⁴⁷J. A. Rayne, Phys. Rev. 133, A1104 (1964); C. K. Jones and J. A. Rayne, in Ref. 45.
- ⁴⁸P. A. Bezuglyi, S. E. Zhevago, and V. I. Denisenko, Zh. Eksp. Teor. Fiz. 49, 1457 (1965) [Sov. Phys.-JETP 22, 1002 (1966)].
- ⁴⁹F. M. Mueller, Phys. Rev. 148, 636 (1966).
- ⁵⁰R. L. Aurbach, J. B. Ketterson, F. M. Mueller, and L. R. Windmiller, Argonne National Laboratory Report No. ANL-7659, Argonne, Ill. 1970 (unpublished). Available from Natl. Tech. Info. Service, U. S. Dept. of Commerce, Springfield, Va. 22151.
- ⁵¹J. B. Ketterson and L. R. Windmiller, Phys. Rev. B 2, 4813 (1970).
- ⁵²J. B. Ketterson and L. R. Windmiller, Phys. Rev. B 1, 463 (1970).
- ⁵³D. E. Soule and J. C. Abele, Phys. Rev. Lett. 23, 1287 (1969).
- ⁵⁴S. W. Hui and J. A. Rayne, Phys. Lett. A 33, 459 (1970); and J. Phys. Chem. Solids 33, 611 (1972).
- ⁵⁵P. T. Coleridge, A. A. M. Croxon, G. B. Scott, and I. M. Templeton, J. Chem. Phys. E 4, 414 (1971); J. E. Schirber and W. J. O'Sullivan, Colloq. Intern. Centre Natl. Rech. Sci. (Paris) 118, 113 (1970); Phys. Rev. B 1, 1443 (1970).
- ⁵⁶N. D. Parada, Ph.D. thesis (MIT, 1968) (unpublished), p. 48.

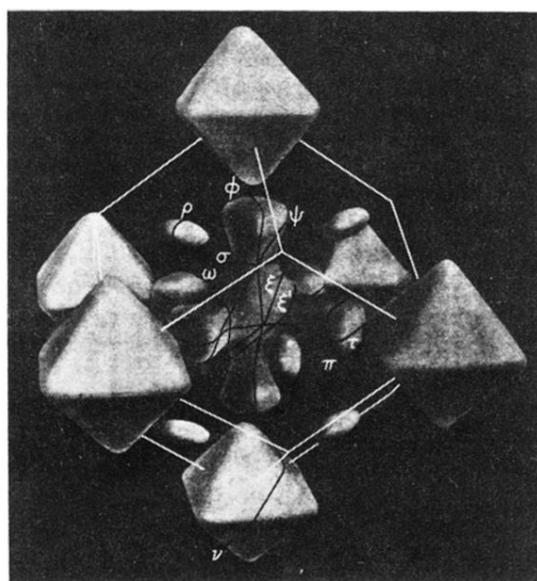


FIG. 1. Perspective sketch of the Fermi surface of W (after Girvan, Gold, and Phillips). The white lines show the Brillouin-zone edges while the dark lines show various extremal orbits. Only the ellipsoids associated with the front faces of the zone are drawn.